



## Synergy of ferric vanadate and MXene for high performance Li- and Na-ion batteries

Huajun Xu<sup>a</sup>, Jiaxing Fan<sup>a</sup>, Di Pang<sup>a</sup>, Yingying Zheng<sup>a</sup>, Gang Chen<sup>a,b</sup>, Fei Du<sup>a,\*</sup>, Yury Gogotsi<sup>c</sup>, Yohan Dall'Agnese<sup>d,\*</sup>, Yu Gao<sup>a,\*</sup>

<sup>a</sup> Key Laboratory of Physics and Technology for Advanced Batteries (Ministry of Education), College of Physics, Jilin University, Changchun 130012, PR China

<sup>b</sup> State Key Laboratory of Superhard Materials, Jilin University, Changchun 130012, PR China

<sup>c</sup> A. J. Drexel Nanomaterials Institute, and Department of Materials Science and Engineering, Drexel University, Philadelphia, PA 19104, United States

<sup>d</sup> Institute for Materials Discovery, University College London, London WC1E 7JE, United Kingdom



### ARTICLE INFO

#### Keywords:

MXene  
Ferric Vanadate  
 $\text{Li}^+/\text{Na}^+$  batteries  
In-situ XRD

### ABSTRACT

Ferric vanadate ( $\text{FeVO}_4$ ) is a desirable anode candidate for lithium-ion battery (LIB) and sodium-ion battery (SIB) because of its high theoretical capacity, low cost and ease of synthesis. However, its practical application is hindered by its volume expansion during the  $\text{Li}^+/\text{Na}^+$  insertion/extraction and low electronic conductivity. Herein, flexible and free-standing  $\text{FeVO}_4/\text{Ti}_3\text{C}_2\text{T}_x$  (FVO/MX) films have been made via combining  $\text{FeVO}_4$  nanorods and  $\text{Ti}_3\text{C}_2\text{T}_x$  MXene sheets via a simple method of vacuum assisted filtration. In the composite films,  $\text{Ti}_3\text{C}_2\text{T}_x$  sheets act as host and  $\text{FeVO}_4$  nanorods are uniformly deposited onto the layers.  $\text{FeVO}_4$  nanorods are encapsulated by  $\text{Ti}_3\text{C}_2\text{T}_x$  sheets, forming a three-dimensional network sandwich structure. The binder-free FVO/MX films exhibited superior electrochemical performance due to the synergy between  $\text{FeVO}_4$  and  $\text{Ti}_3\text{C}_2\text{T}_x$ . Specifically, when FVO/MX electrode was used in a lithium-ion battery, it delivered reversible capacity of 1179  $\text{mAh g}^{-1}$  and 1125  $\text{mAh g}^{-1}$  after 250 cycles at a current density of 0.1  $\text{A g}^{-1}$ . Besides, the FVO/MX = 2:1 anode delivered a reversible capacity of 428  $\text{mAh g}^{-1}$  at 5  $\text{A g}^{-1}$  and 69.5% capacity was retained after 2500 cycles. Moreover, the Na-ion storage capacity reaches 129  $\text{mAh g}^{-1}$  at a high current density of 5  $\text{A g}^{-1}$ , showing capacity retention of 81.1% after 5000 cycles. The charging and discharging mechanism of the FVO/MX based lithiumion battery was studied by *in-situ* XRD technique. Owing to high metallic conductivity and 2D morphology of  $\text{Ti}_3\text{C}_2\text{T}_x$  MXene, 3D networks can be constructed by combining other active agents, suggesting that MXene is a promising host material for the next-generation flexible energy storage devices.

### 1. Introduction

With the rapid development of the high-tech, mobile electronic devices have become essential in people's life, like smart-phones, home appliances, electric vehicle and so on.<sup>[1,2]</sup> Energy storage plays a key role in these technologies. Lithium-ion batteries (LIBs), have high power and energy densities.<sup>[3]</sup> Graphite is the most common commercial anode material for lithium-ion batteries, because of its low price and great cyclability.<sup>[4]</sup> However, the low theoretical capacity of graphite (372  $\text{mAh g}^{-1}$ ) can't satisfy future demands.<sup>[5]</sup> Therefore, researchers have explored many other anodes for lithium-ion batteries. Some materials have much higher theoretical capacity than graphite.<sup>[3,6,7]</sup>

However, they have typically problems such as expensive raw material and/or a complex synthetic route, which seriously hinder their practical application. Much effort is focused on these issues. Take silicon-based lithium-ion batteries as example; silicon has an extraordinary theoretical capacity (4200  $\text{mAh g}^{-1}$ ), but suffers from low conductivity and huge volume expansion/shrinkage during the lithiation/delithiation, resulting in a short life and rapid capacity decline.<sup>[8]</sup> Therefore, researchers have proposed many ideas to solve these problems, such as composites with carbon-based materials (carbon dots, graphite, graphene, rGO) or preparing materials with different morphologies (1D, 2D, porous materials).<sup>[9-13]</sup> Although lithium-ion batteries are widely used in daily life, the resources of metallic lithium on earth are limited,

**Abbreviations:** rGO, Reduced graphene oxide; LIB, Lithium-ion battery; SIB, Sodium-ion battery; XRD, X-ray diffraction; SEM, Scanning electron microscopy; TEM, Transmission electron microscopy.

\* Corresponding authors.

E-mail addresses: [dufei@jlu.edu.cn](mailto:dufei@jlu.edu.cn) (F. Du), [y.dallagnese@ucl.ac.uk](mailto:y.dallagnese@ucl.ac.uk) (Y. Dall'Agnese), [yugao@jlu.edu.cn](mailto:yugao@jlu.edu.cn) (Y. Gao).

<https://doi.org/10.1016/j.cej.2022.135012>

Received 15 December 2021; Received in revised form 13 January 2022; Accepted 29 January 2022

Available online 3 February 2022

1385-8947/© 2022 Published by Elsevier B.V.

so it is necessary to develop another kind of energy storage devices. Sodium-ion batteries (SIBs) have become a new major research direction.<sup>[14,15]</sup> Due to the abundance of sodium, SIBs are suitable for large energy storage facilities, while LIBs are more common in portable devices. In recent years, metal vanadate-based material gradually entered the research field of energy storage due to their advantages of high specific capacity, low cost and easy production. The formula of metal vanadate-based material is  $M_xV_yO_z$ , where M is presents metal element, such as Fe, Cu, Li, and so on.<sup>[16]</sup>  $M_xV_yO_z$  is a promising material for LIBs and SIBs due to its M and V bimetallic composition. They can store lithium ions or sodium ions via redox reactions of M and V ions. M ions can be reduced to metal M ( $M^{n+}$  to  $M^0$ ) and the  $V^{5+}$  can be reduced to  $V^{4+}$ ,  $V^{3+}$ , or even  $V^{2+}$  and  $V^0$ , and this process is usually reversible.<sup>[18]</sup> Many vanadates, such as  $Li_3VO_4$ ,  $FeVO_4$ ,  $CuV_2O_6$ , have been applied in LIBs and other energy storage devices.<sup>[17-21]</sup>  $FeVO_4$  is a cheap material, which has been studied deeply. There are several routes to synthesize  $FeVO_4$ , mostly including hydrothermal and aqueous precipitation methods.<sup>[21,22]</sup>  $FeVO_4$  was first reported and studied in LIBs by Denis *et al* who tested the performance of lithium ions storage and phase change between the lithium ion lithiation/delithiation.<sup>[23]</sup> In addition,  $FeVO_4$  has also been reported as an anode for Na-, K-, Zn-, Mg- and Al-ion batteries.<sup>[24,25]</sup> Xiaolin *et al* studied the modification of  $FeVO_4$  combined with graphene as lithium-ion anodes, and its electrochemical performance reached 1046.5 mAh g<sup>-1</sup> after 100 cycles.<sup>[26]</sup> Besides, an amorphous  $FeVO_4$  was reported as an anode material for potassium-ion battery. In addition to the application of ferric vanadate in a variety of alkaline metal ion batteries, it was also used in high-power sodiumion capacitors, and achieved excellent electrochemical performance.<sup>[27-29]</sup> However,  $FeVO_4$  still faces serious problems of rapid capacity decay and low electronic conductivity.

MXenes, as transition metal carbides, carbonitrides and nitrides, are a large two-dimensional materials family, which are prepared by etching "A" layers from layered carbides, carbonitrides or nitrides known as as MAX phase. The general formula is  $M_{n+1}X_nT_x$  (n = 1–4), where M represents a transition metal, such as Ti, V, Nb and so on; X is C or N and T<sub>x</sub> represents surface terminations, such as -O, -OH, -F and -Cl.<sup>[30]</sup>  $Ti_3C_2T_x$  MXenes have been of great interest for researchers because of their two-dimensional structure, high electronic conductivity (20000 S cm<sup>-1</sup>) and superior hydrophilicity, etc.<sup>[31,32]</sup> Due to their unique structure and excellent performance, MXenes have been applied in energy storage, sensors, catalysis, biomedicine, electromagnetic interference shielding, environment and other fields.<sup>[31,33-35]</sup> Energy storage is the most common research direction at present.<sup>[36]</sup> MXenes can be combined with many other materials due to their rich functional groups and easy dispersion in aqueous solution. The two-dimensional structure allows MXene flakes to be stacked on top of each other, producing flexible and free-standing films via vacuum assisted filtration or rolling.<sup>[37]</sup> That makes MXene a potential candidate for flexible wearable devices. In addition, the two-dimensional structure of MXene can be used as a host for loading other materials, such as silicon nanoparticles, to make flexible electrodes. Xu *et al* used MXene as a binder, for Si, C and their mixture in anode materials of lithium ion and sodium-potassium ion batteries, and the composite materials not only had good flexibility but also showed excellent electrochemical performance.<sup>[38-40]</sup> Zhang *et al* reported that a composited flexible film was prepared with MXene ink and silicon powders.<sup>[41]</sup> Compared with traditional electrode coating on Cu foil, MXene-based flexible film can effectively reduce the weight of the electrode and does not need the conventional binder and current collector.

Given the superior characteristics of MXene, the advantages of MXene can be fully utilized to solve a series of problems, such as the rapid decay of battery capacity. In this paper, we synthesized a unique sandwich structure with MXene as the framework and  $FeVO_4$  loaded between the MXene layers to form a flexible and free-standing electrode film by a simple strategy of vacuum assisted filtration without any binders. The  $FeVO_4$ /MXene flexible membrane is tested as an anode for

LIBs and SIBs. The main intrinsic issues of  $FeVO_4$  are its huge volume expansion, capacity fading and low electronic conductivity. In the  $FeVO_4$ /MXene film,  $FeVO_4$  is embedded between MXene monolayers as an active material, while MXene supports the  $FeVO_4$  particles as a carrier. This structure not only improves the electronic conductivity, but also effectively promotes the ions transport. The two have a synergistic effect. In traditional MXene films, without any additive, layers tend to stack up together because of the van der Waals force, resulting in limited performance.<sup>[42]</sup>  $FeVO_4$  acts as a pillar in the  $FeVO_4$ /MXene film to prevent the stacking of MXene layers. Such special three-dimensional structure of  $FeVO_4$ /MXene can effectively reduce the volume expansion and enhance the stability of electrodes, leading to a longer lifetime of the LIBs and SIBs. At the same time, the conductivity is higher, and it has a better rate performance. Compared with the  $FeVO_4$  electrode coating on the Cu foil with binders (without MXene), the  $FeVO_4$ /MXene electrodes exhibited a superior electrochemical performance, including longer cycle life, greater rate performance and higher capacity.

## 2. Experimental Section

### 2.1. Synthesis of the single layer $Ti_3C_2T_x$ MXene solution

$Ti_3C_2T_x$  MXene was produced by a traditional way of etching the Al layers from  $Ti_3AlC_2$  MAX phase (11 Technology Co., Ltd.) following the previously reported method.<sup>[31]</sup> In short, 5 mL deionized water (DI water) mixed with 15 mL of 12 M HCl, then was added to 1.6 g LiF (Aladdin). After dissolution of LiF, 1 g  $Ti_3AlC_2$  was slowly added into the solution, and stirred for 24 h at 35 °C in oil bath. After 24 h, the solution was transferred to a 50 mL centrifuge tube, then repeatedly centrifuged and washed with DI water until the pH of the suspension reached 6. Single layers of  $Ti_3C_2T_x$  were obtained by vigorously shaking the sediment for 5 min, placing it in ultrasonic bath for 15 mins in Ar atmosphere and ice bath, collecting the suspension, then centrifuging it at 3500 rpm for 15 mins to keep the concentrated (4 mg mL<sup>-1</sup>) single layer  $Ti_3C_2T_x$  sediment.

### 2.2. Synthesis of $FeVO_4$ nanorods

We adopted the previously reported synthesis of  $FeVO_4$  nanorods via a hydrothermal route.<sup>[22]</sup> Following this method, 1 mmol  $Fe(NO_3)_3 \cdot 9H_2O$  (Aladdin) was dissolved in 15 mL of DI water under magnetic stirring for 2 h at room temperature. Then, 1 mmol  $NH_4VO_3$  (Macklin) was dissolved into another 15 mL DI water at 70 °C with oil bath stirring for 2 h. Next,  $NH_4VO_3$  solution was slowly added into  $Fe(NO_3)_3$  solution under magnetic stirring for 30 mins, then transferred into a 50 mL Teflon lined stainless steel autoclave. The autoclave was sealed, heated, and maintained at 160 °C for 5 h to form  $FeVO_4 \cdot xH_2O$ . Once cooled down to room temperature, the sediment was washed via filtration with almost 2 L of DI water and dried in a vacuum oven at 60 °C.  $FeVO_4 \cdot xH_2O$  was sintered at 600 °C for 2 h in air atmosphere with a heating rate of 5 °C per min to obtain the expected product.

### 2.3. Fabrication of free-standing $FeVO_4/Ti_3C_2T_x$ films

The prepared  $FeVO_4$  powder was dispersed in DI water and sonicated for 2 h. Mixtures of  $FeVO_4$  and  $Ti_3C_2T_x$  were prepared simply by mixing corresponding dispersions together under magnetic stirring for 30 mins at room temperature. The  $FeVO_4/Ti_3C_2T_x$  films were fabricated via a simple vacuum assisted filtration of  $FeVO_4/Ti_3C_2T_x$  dispersions. Celgard membranes with a 50 mm diameter and 0.22 μm pore size were used. The films were fabricated with mass ratio of  $FeVO_4$  and MXene of 1:1, 2:1 and 4:1, thus the films were labelled as FVO/MX = 1:1, FVO/MX = 2:1 and FVO/MX = 4:1, respectively. The FVO/MX = 2:1 film thickness was controlled to be about 11 μm. And the density of the film was approximately 1.2 mg/cm<sup>2</sup>. For comparison, an electrode of  $FeVO_4$  was made without  $Ti_3C_2T_x$  MXene, by the conventional doctor blading

method with conventional binders and conductive agent, i.e. coating a slurry of 80 wt%  $\text{FeVO}_4$ , 10 wt% Super-P carbon black and 10 wt% polyvinylidene fluoride in N-methylpyrrolidone onto the Cu foil. This sample is simply denoted as FVO.

#### 2.4. Sample characterizations

The crystal structure of composite films was studied by powder X-ray diffraction (XRD) carried out using a D8 Bruker Advance Diffractometer in the 20 range of 5° to 65° with a Cu K $\alpha$  radiation ( $\lambda = 1.5406 \text{ \AA}$ ). Scanning electron microscopy (SEM) analysis was conducted using a SU8020 equipment from Hitachi. Transmission electron microscopy (TEM) analysis was conducted with a FEI Talos. The X-ray photo-spectroscopy (XPS) was conducted on K-Alpha XPS system and Raman spectroscopy was carried out using a HORIBA HR Evolution Raman spectrometer with a 532 nm diode-pumped solid-state laser.

#### 2.5. Electrochemical measurements

Before use, the full film was dried in a vacuum oven at 80 °C overnight, then electrodes were punched into 63.6 mm<sup>2</sup> disks with a mass loading of about 1.2–1.4 mg, and directly used as anodes in coin cells. The electrochemical studies were performed in CR2032 type coin half-cell assembled in an argon-filled glove box under a low water and oxygen content. For Li-ion battery characterization, Li metal was used as counter and reference electrode, 1 mol L<sup>-1</sup> LiPF<sub>6</sub> dissolved in EC: DMC (1:1, Vol%) was the electrolyte, and Celgard was used as separator. For Na-ion battery tests, Na metal was the counter and reference electrode, glass fiber was used as separator, and 1 mol L<sup>-1</sup> NaClO<sub>4</sub> dissolved in EC: DMC (1:1, Vol%) used as electrolyte. Cyclic voltammetry (CV) was measured between 0.01 and 3 V vs. Li<sup>+</sup>/Li at a scan rate of 0.1 mV s<sup>-1</sup> using an MPG Biologic potentiostat. Electrochemical impedance spectroscopy (EIS) was measured from 1 mHz to 1 MHz on VSP (Biologic-SAS) at open circuit voltages. Capacity retention and rate capability analysis were carried out via galvanostatic charge–discharge tests between 0.01 and 3 V vs. Li<sup>+</sup>/Li using Landt automatic battery tester (Wuhan, China). When measuring long cycle performance at a high current density, the cells were first activated for five pre-cycles with a low current.

### 3. Results and discussion

The preparation of flexible and free-standing  $\text{FeVO}_4/\text{Ti}_3\text{C}_2\text{T}_x$  films is illustrated in Fig. 1a. Briefly,  $\text{Ti}_3\text{C}_2\text{T}_x$  MXene was obtained by selective etching Al layer from  $\text{Ti}_3\text{AlC}_2$  MAX precursor using HCl and LiF,[31] and  $\text{FeVO}_4$  nanorods was synthesized by a simple way of hydrothermal (detailed information is shown in Experimental Section).  $\text{FeVO}_4$  and  $\text{Ti}_3\text{C}_2\text{T}_x$  dispersions were mixed together to obtain a specific mass ratio (FVO/MX = 1:1, FVO/MX = 2:1, FVO/MX = 4:1), then  $\text{FeVO}_4/\text{Ti}_3\text{C}_2\text{T}_x$  electrodes were fabricated via vacuum assisted filtration of that mixture. Consequently, the  $\text{FeVO}_4/\text{Ti}_3\text{C}_2\text{T}_x$  films were flexible, free-standing and without any binders, conductive agent or current collector and the films can serve as anodes for LIBs and SIBs.

The microstructure and morphology of electrode materials were investigated by scanning electron microscopy (SEM). The cross-sectional images of  $\text{FeVO}_4/\text{Ti}_3\text{C}_2\text{T}_x$  are shown in Fig. 1b–d. It's obvious that a “layer-by-layer” morphology with  $\text{FeVO}_4$  nanorods inserted in between horizontally oriented  $\text{Ti}_3\text{C}_2\text{T}_x$  MXene layers to form a 3D open structure. This morphology resulted from self-assembly due to restacking of nanosheets during filtration. The thickness of FVO/MX films was approximately 12  $\mu\text{m}$ , and could be easily controlled by adjusting the amount filtered. Fig S1a demonstrates that the  $\text{FeVO}_4$  nanorods have a length in the range of 3–5  $\mu\text{m}$  with a diameter of approximately 50 nm, and some 20–50 nm diameter nanospheres of  $\text{FeVO}_4$  are embedded in the surface of nanorods which increases the surface area and number of active sites for  $\text{Li}^+/\text{Na}^+$  reactions.  $\text{FeVO}_4$  nanorods act as pillars hindering the compact restacking of MXene nanosheets. And the distribution of Fe, V and O elements indicated that homogeneous  $\text{FeVO}_4$  was successfully synthesized (Fig S1b). With the increased mass ratio of  $\text{FeVO}_4$  in the FVO/MX, the special 3D sandwich structure tends to be more randomly oriented, which might be beneficial for faster insertion/extraction of  $\text{Li}^+/\text{Na}^+$ .[43] Such 3D continuous and uniform structure can be effectively accommodated and accommodate the volume changes during lithiation/delithiation.[44] In addition, the higher magnification of SEM of FVO/MX = 2:1 is shown in Fig. 1e. Owing to the close contact between  $\text{FeVO}_4$  and  $\text{Ti}_3\text{C}_2\text{T}_x$ , the fast electron transport is ensured, which is great for the improvement of electrochemical performance. The optical images of FVO/MX films are exhibited in Fig. 1f. The films colors are gradually darker following increasing the proportion of  $\text{FeVO}_4$ . Moreover, the synthesized films of FVO/MX have a great flexibility, as seen in Fig. 1g. The flexibility is attributed to  $\text{Ti}_3\text{C}_2\text{T}_x$  sheets.

To further characterize the films obtained, X-ray diffraction (XRD)

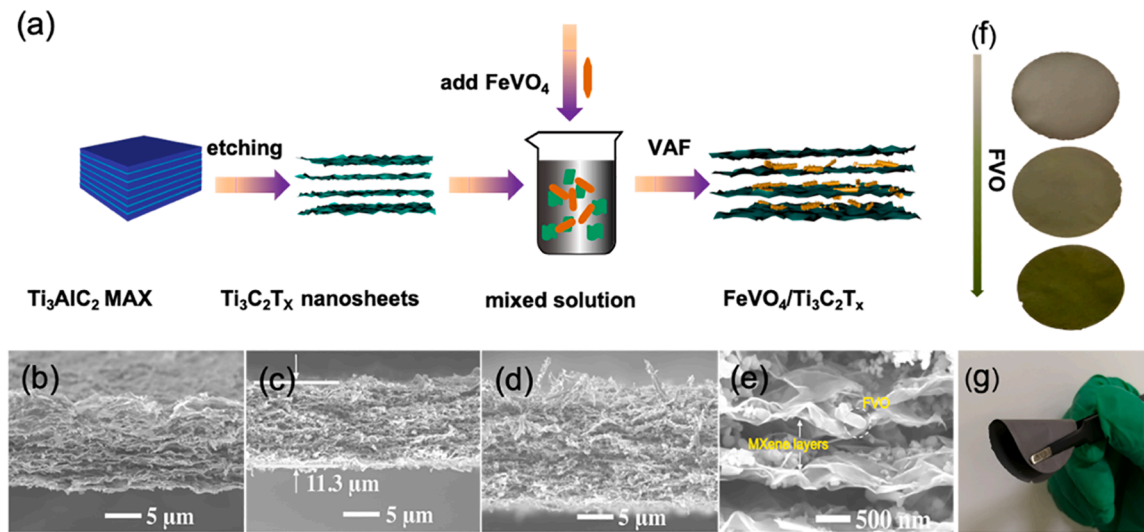


**Fig. 1.** Schematic illustration of the synthetic procedure of FVO/MX films composites. (a) Schematic representation of the preparation method of FVO/MX films composites. Cross-sectional scanning electron microscopy images of (b) FVO/MX = 1:1, (c) FVO/MX = 2:1, (d) FVO/MX = 4:1 and (e) FVO/MX = 2:1. Optical images of (f) prepared FVO/MX composites with different mass ratio for 1:1, 2:1, 4:1, respectively. (g) Flexible illustration for FVO/MX = 2:1 film.

was used and recorded patterns are shown in Fig. 2a along with the FeVO<sub>4</sub> reference XRD pattern (PDF 71–1592). The peaks of pure Ti<sub>3</sub>C<sub>2</sub>T<sub>x</sub> film were located at 7.2° and 14.5°, corresponding to (002) and (004) reflections, which demonstrates well delaminated Ti<sub>3</sub>C<sub>2</sub>T<sub>x</sub> MXene sheets.[32] The FeVO<sub>4</sub> nanorods pattern presents two main peaks at 20≈25.1° and ≈27.8° corresponding to the (012) and (1–12) peaks.[22] In the FVO/MX film, the typical (002) peak of Ti<sub>3</sub>C<sub>2</sub>T<sub>x</sub> and (012), (0–22) peaks of FeVO<sub>4</sub> were present. The most intense (002) peak of Ti<sub>3</sub>C<sub>2</sub>T<sub>x</sub> was located at 6.3°, corresponding to an interlayer spacing of 14.0 Å, compared with the (002) peak (d-lattice is 12.2 Å) of pure Ti<sub>3</sub>C<sub>2</sub>T<sub>x</sub> film, meaning the FVO/MX films have larger interlayer spacing which might facilitate Li<sup>+</sup>/Na<sup>+</sup> insertion/extraction during the redox reaction process. The (002) peaks in FVO/MX films were broader than in pure Ti<sub>3</sub>C<sub>2</sub>T<sub>x</sub>, which suggests less restacked and more randomly oriented wrinkled layers of Ti<sub>3</sub>C<sub>2</sub>T<sub>x</sub>. The peak intensity of Ti<sub>3</sub>C<sub>2</sub>T<sub>x</sub> decreased from FVO/MX = 1:1 to FVO/MX = 4:1, owing to the decrease of Ti<sub>3</sub>C<sub>2</sub>T<sub>x</sub> content.

X-ray photoelectron spectroscopy (XPS) was used to investigate the surface chemistry and chemical state of the elements of the FVO/MX = 2:1 film, especially Fe, V and Ti. Additionally, the Ti and V XPS spectra of FeVO<sub>4</sub> alone are shown in Fig S3, which were consistent with previous work.[21] The Fe 2p and V 2p spectra of FVO/MX = 2:1 was similar to the raw FeVO<sub>4</sub> nanorods. However, the intensity of Fe 2p XPS spectrum in Fig. 2b was lower than in pristine FeVO<sub>4</sub>, probably due to less FeVO<sub>4</sub> exposed on the surface of FVO/MX = 2:1. Fe 2p spectrum was divided into 3 peaks corresponding Fe<sup>3+</sup> 2p<sub>1/2</sub>, Fe<sup>3+</sup> 2p<sub>3/2</sub>, and one satellite peak, located respectively at 712.1 eV, 725.5 eV and 733.6 eV. The Fe 2p peaks were the same as the precursor FeVO<sub>4</sub>. The V 2p region in Fig. 2c was clearly overlapped with the FeVO<sub>4</sub> film. The Ti XPS spectrum of FVO/MX = 2:1 is shown Fig. 2d. The Ti 2p can be fitted with 3 doubles, Ti-C, Ti<sup>2+</sup> and Ti<sup>3+</sup>. The 3 pairs of the peak was located at (455.2 eV, 460.6 eV), (456.5 eV, 461.5 eV) and (458.7 eV, 463.2 eV), respectively,

and the peaks are consistent with previous work.[45] Besides, there is no unexpected shift of peaks indicating the well preserved compositions of FeVO<sub>4</sub> and Ti<sub>3</sub>C<sub>2</sub>T<sub>x</sub>.

In order to verify the combination of the FeVO<sub>4</sub> and Ti<sub>3</sub>C<sub>2</sub>T<sub>x</sub> MXene, Raman spectroscopy analysis was performed (Fig S4a), including FVO and FVO/MX films. The FeVO<sub>4</sub> alone has several main peaks in the range of 500 – 1000 cm<sup>-1</sup>, consistent with results in the literature.[46] For the FVO/MX film, the peak intensity of FeVO<sub>4</sub> was lower than FVO, which is attributed to MXene sheets covering most of the FeVO<sub>4</sub> nanorods. The peak intensity of FVO/MX = 4:1 sample was contrary to FVO/MX = 1:1 and 2:1, that should be due to more FeVO<sub>4</sub> present. Such phenomenon is consistent with the microstructure of FVO/MX film (FeVO<sub>4</sub> and MXene were disorderly distributed on the surface of the FVO/MX = 4:1 film, as we discussed above). The Raman peak centered around 198.8 cm<sup>-1</sup> in FVO/MX = 4:1 is attributed to the Ti<sub>3</sub>C<sub>2</sub>T<sub>x</sub> MXene as it is the same peak as in the Ti<sub>3</sub>C<sub>2</sub>T<sub>x</sub> film alone (shown in Fig S2) consistent to previous work.[47] The Raman peak located at 1581.1 cm<sup>-1</sup> represents the graphitic carbon band (G-band) which decreases gradually with the Ti<sub>3</sub>C<sub>2</sub>T<sub>x</sub> amount.

To further investigate the microstructure of the FVO/MX = 2:1, transmission electron microscopy (TEM) analysis was conducted and shown Fig. 3. Ti<sub>3</sub>C<sub>2</sub>T<sub>x</sub> sheets were found in Fig. 3a, b, and FeVO<sub>4</sub> nanorods laid on the sheets and some FeVO<sub>4</sub> nanospheres can be seen as well in the layers. Meanwhile, a FeVO<sub>4</sub> porous structure may be formed during the high temperature sintering process.[24] High-resolution TEM (HRTEM) lattice images in Fig. 3c,d show lattice spacing of 0.32 and 0.35 nm, corresponding to (012) and (0–22) plane of FeVO<sub>4</sub>.[22,25] Besides, Ti<sub>3</sub>C<sub>2</sub>T<sub>x</sub> nanosheets can be observed in Fig. 3c. A contact between FeVO<sub>4</sub> and Ti<sub>3</sub>C<sub>2</sub>T<sub>x</sub> is good for electron transfer which can effectively improve the rate performance of Li/Na ion batteries.

To further systematically evaluate the electrochemical performance of the FVO/MX electrodes in Li-ion battery, a series of electrochemical

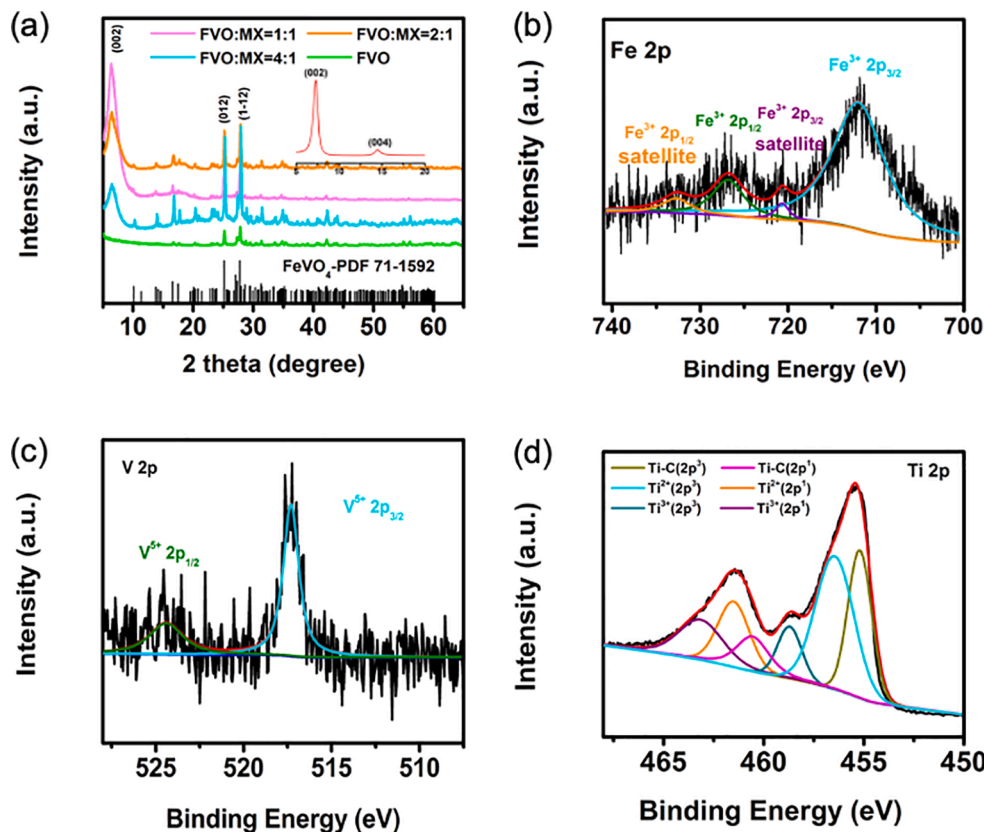


**Fig. 2.** Structure characterization of the FVO/MX films. a) XRD patterns of FVO/MX films and FeVO<sub>4</sub> powders. (Inset: Ti<sub>3</sub>C<sub>2</sub>T<sub>x</sub> MXene XRD pattern.) High resolution XPS of FVO/MX = 2:1 in the b) Fe 2p, c) V 2p and d) Ti 2p regions.

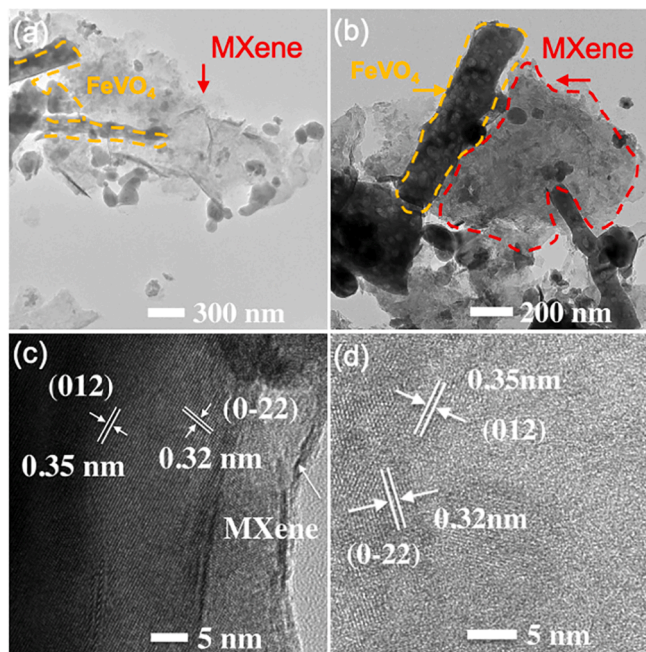
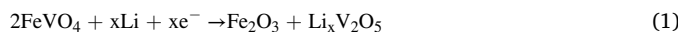


**Fig. 3.** Morphological and microstructure characterization of FVO/MX = -2:1. a, b) TEM and c, d) Highresolution TEM images.

tests were performed. Fig. 4a shows the lithiation/delithiation phenomenon of FVO/MX = 2:1 via CV during the first five cycles at a scan rate of  $0.1 \text{ mV s}^{-1}$ . During the first cycle, there is an obvious reduction peak located at  $0.217 \text{ V}$  which is not present in the following cycles thus can be attributed to the formation of solid-electrolyte interface (SEI). [48,49] Besides, the reduction peak at  $0.45 \text{ V}$  can be found, which can be ascribed to the initial reduction of  $\text{FeVO}_4$  to  $\text{Fe}_2\text{O}_3$  and lithium vanadates following the process of reduction of  $\text{V}^{5+}$  to  $\text{V}^{4+}$ , and  $\text{V}^{3+}$  even  $\text{V}^0$ . The reduction peak shifted to the right on following cycles. When Li ion are inserted into a  $\text{FeVO}_4$  crystal, there is an irreversible phase reaction happening; the triclinic  $\text{FeVO}_4$  transforms into iron oxide and lithium vanadates and finally forms into  $\text{Li}_2\text{O}$ ,  $\text{Fe}$  and even  $\text{V}$ .[23] The possible electrochemical reactions upon lithiation/delithiation are proposed as follows:



The full equation can be written as:



Such process leads to an irreversible reduction reaction and the peak shifts to right. Two main oxidation peaks were observed around at  $1.3$  and  $2.0 \text{ V}$ . Those peaks are mainly attributed to the delithiation of Li ions from  $\text{Li}_{x+y}\text{V}_2\text{O}_5$ . Theoretically,  $8\text{Li}^+$  can be accommodated by the  $\text{FeVO}_4$  to form  $\text{Li}_2\text{O}$ ,  $\text{Fe}$  and  $\text{V}$ .[23] Besides, the above-mentioned two oxidation peaks were still found in the following cycling tests, which demonstrates the reversible extraction of Li ion. The galvanostatic charge/discharge curves of the first five cycles of FVO/MX = 2:1 for LIBs at  $0.1 \text{ A g}^{-1}$  are displayed in Fig. 4b. During the first cycle, the electrode of FVO/MX = 2:1 exhibits a high discharge specific capacity of  $1432 \text{ mAh g}^{-1}$  and achieves an initial Coulombic efficiency of  $80.5\%$ . During the following cycles, the curves almost overlapped together which presents a highly reversible capacity and insertion/extraction of Li ions. The electrodes were tested at different rates and the reversible capacities of FVO/MX =

2:1 are  $1426 \text{ mAh g}^{-1}$ ,  $1106 \text{ mAh g}^{-1}$ ,  $1006 \text{ mAh g}^{-1}$ ,  $911 \text{ mAh g}^{-1}$ ,  $816 \text{ mAh g}^{-1}$  and  $696 \text{ mAh g}^{-1}$  at  $0.1 \text{ A g}^{-1}$ ,  $0.2 \text{ A g}^{-1}$ ,  $0.5 \text{ A g}^{-1}$ ,  $1 \text{ A g}^{-1}$ ,  $2 \text{ A g}^{-1}$  and  $5 \text{ A g}^{-1}$ , respectively, as shown in Fig. 4c. The same oxidation-reduction reaction plateau was found at different current densities, which demonstrates the reversible process and good rate capability of lithiation/delithiation of this electrode.

The reaction kinetics was investigated by electrochemical impedance spectroscopy (EIS). The EIS of  $\text{FVO}/\text{MX} = 1:1$ ,  $\text{FVO}/\text{MX} = 2:1$ ,  $\text{FVO}/\text{MX} = 4:1$  and  $\text{FVO}$  electrodes were compared in Fig. 4d. The inset is equivalent circuit diagram. The first intercept corresponds to the electrolyte resistance ( $R_e$ ). The semicircle in the high frequency region represents the charge transfer resistance between the electrolyte and interface of electrode ( $R_{ct}$ ). The low frequency area with a  $45^\circ$  angle is related to the ion diffusion limitation within the electrode.[50] In the Nyquist plots shown, the  $R_{ct}$  values were  $427 \Omega$ ,  $210 \Omega$ ,  $535 \Omega$  and  $1164 \Omega$  for  $\text{FVO}/\text{MX} = 1:1$ ,  $\text{FVO}/\text{MX} = 2:1$ ,  $\text{FVO}/\text{MX} = 4:1$  and  $\text{FVO}$  anodes. Overall  $\text{FVO}/\text{MX}$  composites have lower charge transfer resistance than the  $\text{FVO}$  electrode, corroborating that the expected advantages of this structure, including better electrolyte percolation and increased conductivity due to  $\text{Ti}_3\text{C}_2\text{T}_x$  sheets. The EIS results of  $\text{FVO}/\text{MX} = 2:1$  film shows the lowest impedance, fastest electron transport and superior stability. To further study the electronic properties, the electronic conductivities of the  $\text{FVO}/\text{MX}$  films were measured and results are shown in Table S1. The electronic conductivity values of  $\text{FVO}/\text{MX} = 1:1$ ,  $\text{FVO}/\text{MX} = 2:1$ ,  $\text{FVO}/\text{MX} = 4:1$  are  $97 \text{ S cm}^{-1}$ ,  $40 \text{ S cm}^{-1}$  and  $14 \text{ S cm}^{-1}$ , respectively. That is higher than  $\text{FVO}$  ( $5 \times 10^{-5} \text{ S cm}^{-1}$ ) reported in previous work.[51] The electronic conductivity of  $\text{FVO}/\text{MX}$  films further verifies improvement of the electrodes by combining the oxide with MXene.

In the Fig. 4e, the rate performance of  $\text{FVO}/\text{MX}$  electrodes and  $\text{FVO}$  was further explored at an increasing current density. It's clear that the  $\text{FVO}/\text{MX} = 2:1$  electrode has the highest discharge capacity among them. Besides,  $\text{FVO}/\text{MX} = 1:1$  and  $\text{FVO}/\text{MX} = 4:1$  electrodes also effectively enhanced the capacity of the cell owing to their higher conductivity and special sandwich morphology. The electrode of  $\text{FVO}/\text{MX} = 2:1$  delivers high discharge capacities, as discussed in Fig. 4c, and interestingly recovers high capacities of  $719 \text{ mAh g}^{-1}$ ,  $824 \text{ mAh g}^{-1}$ ,  $877 \text{ mAh g}^{-1}$ ,  $926 \text{ mAh g}^{-1}$ ,  $955 \text{ mAh g}^{-1}$  when going back to  $2 \text{ A g}^{-1}$ ,  $1 \text{ A g}^{-1}$ ,  $0.5 \text{ A g}^{-1}$ ,  $0.2 \text{ A g}^{-1}$ , and  $0.1 \text{ A g}^{-1}$ , respectively, showing good rate capability. Moreover, when the current density was  $5 \text{ A g}^{-1}$ , the capacity of the  $\text{FVO}/\text{MX} = 2:1$  achieved a capacity retention of  $48.8\%$  when the current density increased from  $0.1 \text{ A g}^{-1}$  to  $5 \text{ A g}^{-1}$ . On contrary, the performance of the  $\text{FVO}$  electrode is fading quickly with increasing rate, with about zero at  $1 \text{ A g}^{-1}$ . This may be attributed to the low electronic conductivity and volume expansion drawbacks.

Cycling stability of the  $\text{FVO}/\text{MX}$  and  $\text{FVO}$  electrodes was compared at a current density of  $0.1 \text{ A g}^{-1}$ , as shown in Fig. 4f. The  $\text{FVO}/\text{MX} = 2:1$  anode delivered the highest capacity of  $1125 \text{ mAh g}^{-1}$  after 250 cycles and the capacity retention was  $106\%$ . That is much higher than the other three anodes including  $\text{FVO}/\text{MX} = 1:1$  ( $849 \text{ mAh g}^{-1}$ ),  $\text{FVO}/\text{MX} = 4:1$  ( $934 \text{ mAh g}^{-1}$ ) and  $\text{FVO}$  ( $491 \text{ mAh g}^{-1}$ ). Specifically, the capacity of  $\text{FVO}$  anode faded quickly below  $100 \text{ mAh g}^{-1}$  due to the volume expansion of the  $\text{FeVO}_4$  nanorods during the lithiation/delithiation progress and the conventional PVDF binders also can't prevent the active agent fall from the current collector. Compared with  $\text{FVO}$  anode,  $\text{FVO}/\text{MX}$  electrode maintained a great cycling performance, the fading was slower, which can be linked to the 3D sandwich structure. When Li ions react with  $\text{FeVO}_4$ , there is a large volume expansion, but there is enough space between  $\text{Ti}_3\text{C}_2\text{T}_x$  MXene sheets to encapsulate  $\text{FeVO}_4$  nanorods and mitigate the enlarged volume. Such structure can also improve the stability of the electrode because  $\text{FeVO}_4$  nanoparticles are trapped inside the  $\text{Ti}_3\text{C}_2\text{T}_x$  layers which stops the usual issue of disconnection from current collector. It is worth mentioning that the capacity is increasing after approximately 80 cycles until 250 cycles. The increasing capacity may be attributed to the reversible formation of a polymeric gel-like interface on the electrode as a result of kinetically

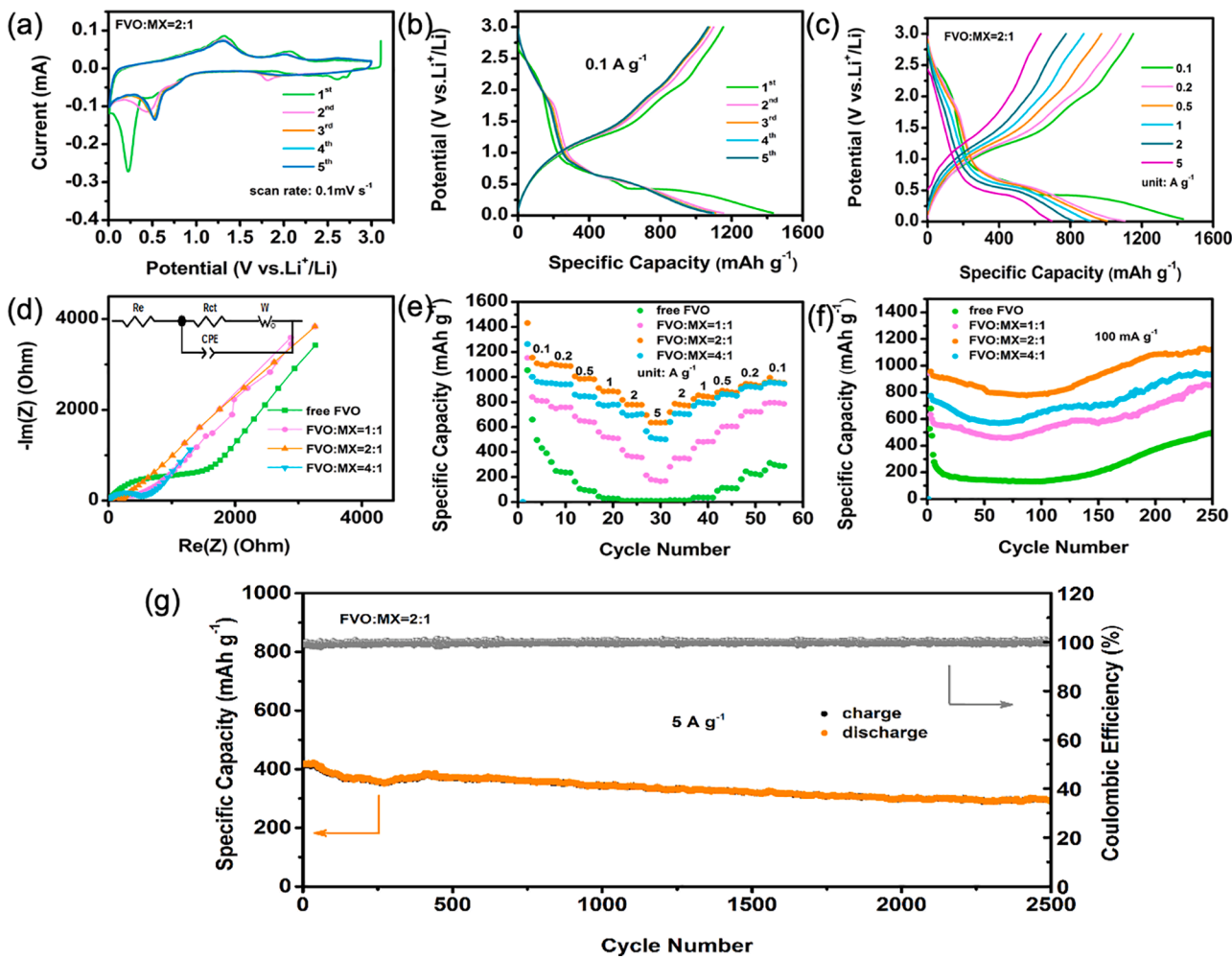


**Fig. 4.** Electrochemical Li-ion storage behavior of FVO/MX and FVO electrodes. a) Cyclic voltammograms of the initial five cycles at  $0.1 \text{ mV s}^{-1}$ . Charge and discharge curves of FVO/MX = 2:1; b) at  $0.1 \text{ A g}^{-1}$  and c) at different current density from  $0.1 \text{ A g}^{-1}$  to  $5 \text{ A g}^{-1}$ . d) Nyquist curves of FVO/MX electrodes (Inset: equivalent circuit diagram). e) Rate performance and f) cycling performance at  $100 \text{ mA g}^{-1}$  of the prepared electrodes. g) long cycling test of FVO/MX = 2:1 at  $5 \text{ A g}^{-1}$ .

activated electrolyte degradation, such phenomenon is commonly observed on the transition metal oxides, such as  $\text{Fe}_2\text{O}_3$ ,  $\text{Fe}_3\text{O}_4$  and  $\text{MnO}$ . [52-54]

SEM images of FVO and FVO/MX = 2:1 electrode after 250 cycles are shown in Fig S5 which can be compared to SEM images before cycling, such as seen Fig S1. It was found that the FVO was subjected to pulverization during cycling, evidenced by the presence of very large aggregates, breakdown of nanorods and growth of the SEI layer.[55] Compared with the FVO electrode, the surface of the FVO/MX = 2:1 electrode also shows evidence of pulverization but appears more homogeneous and in close contact, which can improve the electron transport path.

To further evaluate the long-cycling performance, the capacity retention and Coulombic efficiency of FVO/MX = 2:1 electrode was tested at high current density of  $5 \text{ A g}^{-1}$  (Fig. 4g) and at  $2 \text{ A g}^{-1}$  (Fig S6). Note that long cycling experiments with the larger current density were conducted after first five cycles activated at  $0.1 \text{ A g}^{-1}$ . The FVO/MX = 2:1 anode delivered an initial capacity of  $418 \text{ mAh g}^{-1}$  at  $5 \text{ A g}^{-1}$ , and maintained a capacity of  $291 \text{ mAh g}^{-1}$ , that is a capacity retention of 69.5%. The Coulombic efficiency after 2500 cycles was 99.4 %. Both the high Coulombic efficiency and high-capacity retention reflect stable cycling performance. Similar promising results were achieved at  $2 \text{ A g}^{-1}$  as the initial capacity was  $743 \text{ mAh g}^{-1}$  and it decreased to  $483 \text{ mAh g}^{-1}$  after 2500 cycles.

The promising electrochemical performance prompted us to explore the  $\text{Li}^+$  storage behavior in the FVO/MX = 2:1 electrode in depth. Besides,  $\text{Ti}_3\text{C}_2\text{T}_x$  can provide significant pseudocapacitive storage contribution coming from the surface redox reaction, which co-operate with battery-like faradaic process of  $\text{FeVO}_4$  in the FVO/MX = 2:1 electrode. [56] The contributions of capacitive and diffusion-controlled processes were further studied in Fig. 5a by analysis of CV curves at sweep rates of  $0.1 \text{ mV s}^{-1}$ ,  $0.2 \text{ mV s}^{-1}$ ,  $0.5 \text{ mV s}^{-1}$ ,  $1 \text{ mV s}^{-1}$  and  $2 \text{ mV s}^{-1}$ . Normally, in this type of electrode material, we would expect three main  $\text{Li}^+$  storage mechanisms including: (1) diffusion-controlled contribution coming from conversion reaction; (2) pseudocapacitive contribution coming from the surface fast redox reaction and fast intercalation; and (3) capacitive contribution based on the electrochemical double layer formation.[57] The capacitive contributions (including pseudocapacitance and double layer) and diffusion-controlled contribution can be calculated by the relationship between the measured peak current ( $I$ ) and the scan rate ( $v$ ), which satisfies the following formula:

$$i = av^b \quad (6)$$

where  $a$  and  $b$  are parameters that can be experimentally determined. Generally,  $b = 0.5$  means a diffusion-controlled process which corresponding to the battery-type material,  $b = 1$  corresponding to a capacitive surface-controlled process leading to the supercapacitor-type material.[58,59] When  $b$  is between 0.5 and 1, the material shows a

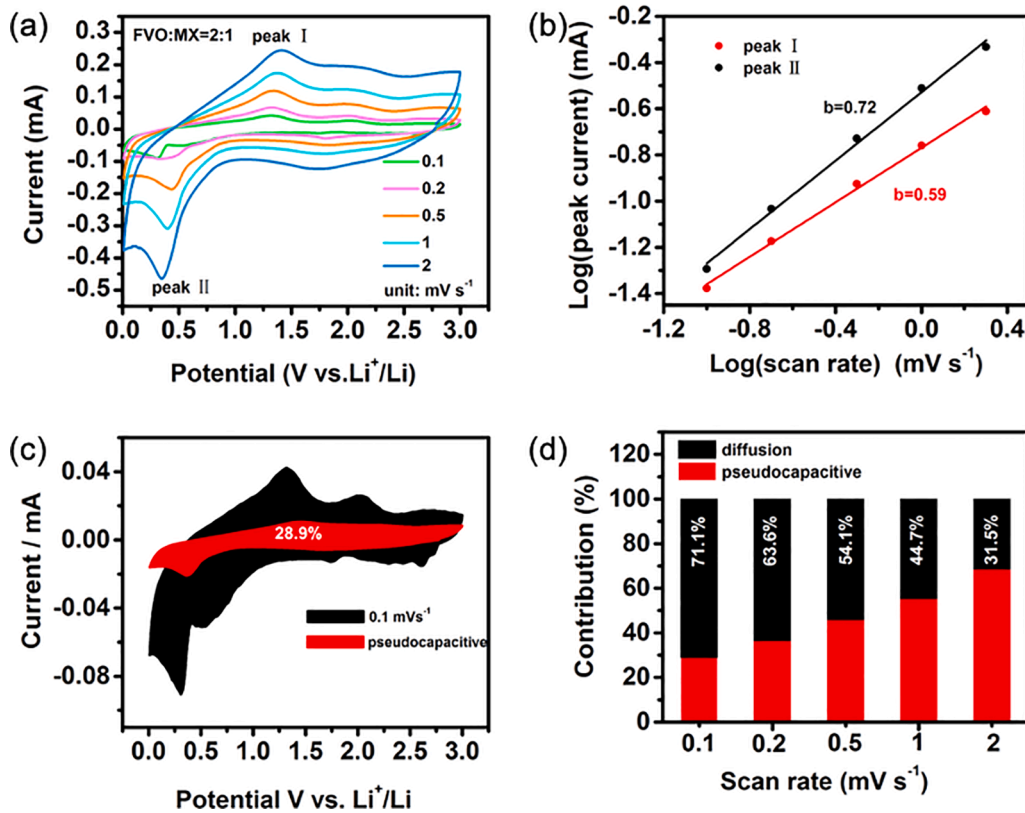


**Fig. 5.** Kinetics analysis of the electrochemical behavior of FVO/MX = 2:1 electrode. a) CV curves at different scan rate ( $0.1\text{--}2\text{ mV s}^{-1}$ ). b) Relationship between peak current and scan rate. d) CV curve with corresponding pseudocapacitive contribution at  $0.1\text{ mV s}^{-1}$ . d) Pseudocapacitive contribution ratios at different sweep rate.

mixed behavior resulting from both types of processes occurring in parallel. According to the Fig. 5b, the  $b$  values of the anodic (peak I) and the cathodic (peak II) were calculated by linear fitting to be 0.72 and 0.59, confirming that the capacity of FVO/MX = 2:1 comes from both, diffusion-controlled and capacitive processes. To further study the capacitive and diffusion contributions, complementary analysis was conducted using the following relationship between the current value ( $i$ ) at fixed voltage, capacitive contribution ( $k_1v$ ), and diffusion contribution ( $k_2v^{1/2}$ ):[58]

$$i(v) = k_1v + k_2v^{1/2} \quad (7)$$

As shown in Fig. 5c, there is 28.9% of capacitive contribution to the whole Li ion storage at the scan rate of  $0.1\text{ mV s}^{-1}$ . As expected, the capacitive contribution gradually increased with the increasing scan rate, up to 68.5% at  $2\text{ mV s}^{-1}$ . This might be attributed to the too slow conversion mechanism which is not fully achieved at higher rates and some particles might not be accessible for  $\text{Li}^+$  storage.

To further reveal the  $\text{Li}^+$  storage mechanism and phase transformation of FVO/MX = 2:1 in LIBs, in-situ XRD was carried out, shown in Fig. 6. The in-situ XRD analysis was performed at  $2\theta$  range from  $5^\circ$  to  $40^\circ$  and recorded at various potentials during cycling. In the in-situ XRD pattern, the typical (002) peak of MXene was not present. This is due to the Be window, with a strong background peak of Be masking the (002) peak of MXene. In the discharge process, the (1-12) peak had a progressive and continuous shift to the higher value. (1-12) peak shifted from  $27.9^\circ$  to  $28.4^\circ$  during the discharge from  $2.90\text{ V}$  to  $0.45\text{ V}$ . The (012) peak shifted left, indicating triclinic  $\text{FeVO}_4$  transformed into  $\text{Li}_{x+y}\text{V}_2\text{O}_5$  and followed by  $\text{Li}_{x+y}\text{V}_2\text{O}_5$ .[22] Finally, the  $\text{FeVO}_4$  should be transformed the  $\text{Li}_2\text{O}$ , Fe and V, according to the CV profiles and the actual specific capacity achieved. The presence of iron oxide can be found when the discharge voltage reaches  $0.4\text{ V}$ . However, we did not find peaks of Fe, V or  $\text{Li}_2\text{O}$ . Besides, during the charge process, the

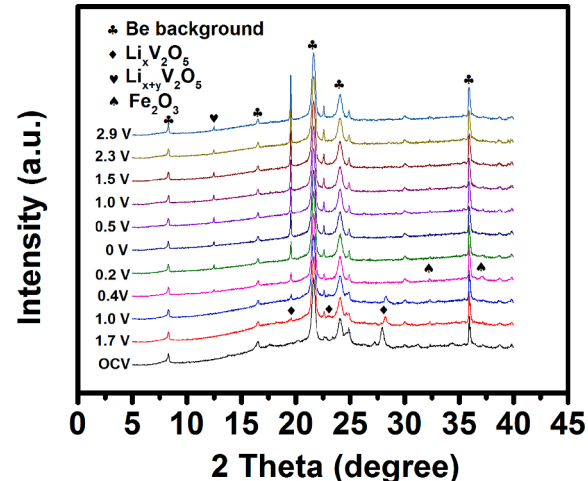


**Fig. 6.** In-situ XRD analysis of FVO/MX = 2:1 electrode for lithium-ion battery.

(1-12) peak vanished and didn't show up again, indicating the irreversible process of lithium-ion intercalation in the first cycle, which is one reason for the capacity decay in the first cycle. The presence of iron oxide can also be a reason for the increasing capacity during the long cycle test. In order to better explain the change of partial peak position and irreversibility of the first cycle, the in-situ XRD contour picture is shown in Fig S7. We can clearly see that the (1-12) peak moved from  $27.9^\circ$  to  $28.4^\circ$  and then disappeared.

Both,  $\text{Ti}_3\text{C}_2\text{T}_x$  and  $\text{FeVO}_4$  individually, previously showed attractive behavior in  $\text{Na}^+$  storage. Hence we decided to evaluate the electrochemical behavior of our composite for sodium ion batteries.

[25,31] Just like in the  $\text{Li}^+$  battery, the as-prepared FVO/MX film without any binders or current collector was used as the working electrode. Fig. 7a shows the first five CV cycles of the FVO/MX = 2:1 electrode. In the first cycle, there are two reduction peaks located at 0.68 V and 0.83 V. These cathodic current peaks are irreversible and can be attributed to the formation of solid electrolyte interphase (SEI). [21,25] After the first cycle, there is one pair of redox peaks present in the subsequent cycles, corresponding to the reversible sodiation/desodiation of  $\text{FeVO}_4$ . To test the rate capability of this electrode, both CV scans at different scan rates ( $0.1 \text{ mV s}^{-1}$  to  $2 \text{ mV s}^{-1}$ ) and galvanostatic charge-discharge experiments at different current densities ( $0.1 \text{ A g}^{-1}$  to  $10 \text{ A g}^{-1}$ ) were performed. The reversible pair of redox reactions are observed in both tests shown in Fig. 7b and 7c. In the cyclic voltammograms, the peak positions don't shift significantly at higher rates, indicating a low overpotential, good electrochemical activity and reversible process. In the charge-discharge curves, as well as the calculated capacity shown Fig. 7d, we can observe the promising discharge capacity of  $543 \text{ mAh g}^{-1}$ ,  $280 \text{ mAh g}^{-1}$ ,  $235 \text{ mAh g}^{-1}$ ,  $210 \text{ mAh g}^{-1}$ ,  $181 \text{ mAh g}^{-1}$ ,  $153 \text{ mAh g}^{-1}$ ,  $98 \text{ mAh g}^{-1}$  and  $231 \text{ mAh g}^{-1}$ , at varying current densities of  $0.1 \text{ A g}^{-1}$ ,  $0.2 \text{ A g}^{-1}$ ,  $0.5 \text{ A g}^{-1}$ ,  $1 \text{ A g}^{-1}$ ,  $2 \text{ A g}^{-1}$ ,  $5 \text{ A g}^{-1}$ ,  $10 \text{ A g}^{-1}$  then back to  $0.1 \text{ A g}^{-1}$ , respectively. Moreover, when the current density was  $10 \text{ A g}^{-1}$ , the FVO/MX = 2:1 anode had a higher capacity of  $98 \text{ mAh g}^{-1}$  with the 99.8% Coulombic efficiency (Fig. 7d). Compared with the state-of-the-art hard carbon, FVO/MX = 2:1 electrode shows a higher capacity and high-rate performance, which can be attributed to the 3D sandwich structure and excellent conductivity of the FVO/MX = 2:1 film. In order to prove the excellent performance of FVO/MX in sodium ion battery, we prepared FVO and  $\text{Ti}_3\text{C}_2\text{T}_x$  electrodes for comparison, and the results proved that the FVO/MX composite can effectively improve the electrochemical performance of the electrode, as shown in Fig S8a.

Owing to the great rate performance of FVO/MX = 2:1 electrode applied in SIBs, to better evaluate the long-life property in SIBs, the long cycling was tested at a current density of  $5 \text{ A g}^{-1}$  shown in Fig. 7e. Before long cycling tests, the cell underwent 3 pre-cycles at  $0.1 \text{ A g}^{-1}$ . The Na ion storage capacity obtained in the first cycle at  $5 \text{ A g}^{-1}$  was  $129 \text{ mAh g}^{-1}$ . After 5000 cycles, a capacity of  $105 \text{ mAh g}^{-1}$  remained, proving a

capacity retention of 81.1%, with a Coulombic efficiency of 99.52%. Additionally, a long cycling test at a current density of  $2 \text{ A g}^{-1}$  was also performed and shown in Fig S8b. The first discharge capacity reached  $181 \text{ mAh g}^{-1}$ , and  $141 \text{ mAh g}^{-1}$  remained after 2000 cycles, with a Coulombic efficiency of 98.3%. Such encouraging performance of FVO/MX = 2:1 electrode in SIBs originates from its structure and high conductivity, giving a great stability of FVO/MX = 2:1 electrode.

#### 4. Conclusion

To conclude, we successfully fabricated flexible and free-standing  $\text{FeVO}_4/\text{Ti}_3\text{C}_2\text{T}_x$  films combining  $\text{FeVO}_4$  nanorods and  $\text{Ti}_3\text{C}_2\text{T}_x$  MXene nanosheets via a simple method of vacuum assisted filtration. The FVO/MX films were directly used as anodes for LIBs and SIBs, and exhibited superior electrochemical performance due to the synergy between  $\text{FeVO}_4$  and  $\text{Ti}_3\text{C}_2\text{T}_x$ . In the FVO/MX composites,  $\text{Ti}_3\text{C}_2\text{T}_x$  sheets acted as a pseudocapacitive conductive host and battery-type material  $\text{FeVO}_4$  nanorods were uniformly laid in between the layers. This structure can effectively improve the space available to accommodate the volume expansion in the process of  $\text{Li}^+/\text{Na}^+$  reactions while the close contact between  $\text{FeVO}_4$  and  $\text{Ti}_3\text{C}_2\text{T}_x$  can effectively improve the electron transport. Owing to the special 3D structure, even if pulverization occurs in the reaction with  $\text{Li}^+/\text{Na}^+$ ,  $\text{FeVO}_4$  nanorods would still keep contact with  $\text{Ti}_3\text{C}_2\text{T}_x$  layers, which is good for the cycling stability. Among the three FVO/MX films with different mass ratios, FVO/MX = 2:1 delivered the best performance. Specifically, when FVO/MX = 2:1 electrode was used for the lithium-ion battery, it delivered an initial reversible capacity of  $1179 \text{ mAh g}^{-1}$  and retained  $1125 \text{ mAh g}^{-1}$  after 250 cycles at a current density of  $0.1 \text{ A g}^{-1}$ . Besides, the FVO/MX = 2:1 anode delivered a reversible capacity of  $418 \text{ mAh g}^{-1}$  in the first cycle, and retained  $291 \text{ mAh g}^{-1}$  with 99.4 % Coulombic efficiency after 2500 cycles, and 69.5% capacity remained at  $5 \text{ A g}^{-1}$  current density in LIBs. Compared with the conventional FVO electrodes, FVO/MX films can effectively mitigate the common drawbacks of conversion reaction materials and improve the cycling stability and electrochemical performance. These films can be directly used as anodes for batteries and be used in next-generation flexible and wearable energy storage devices.

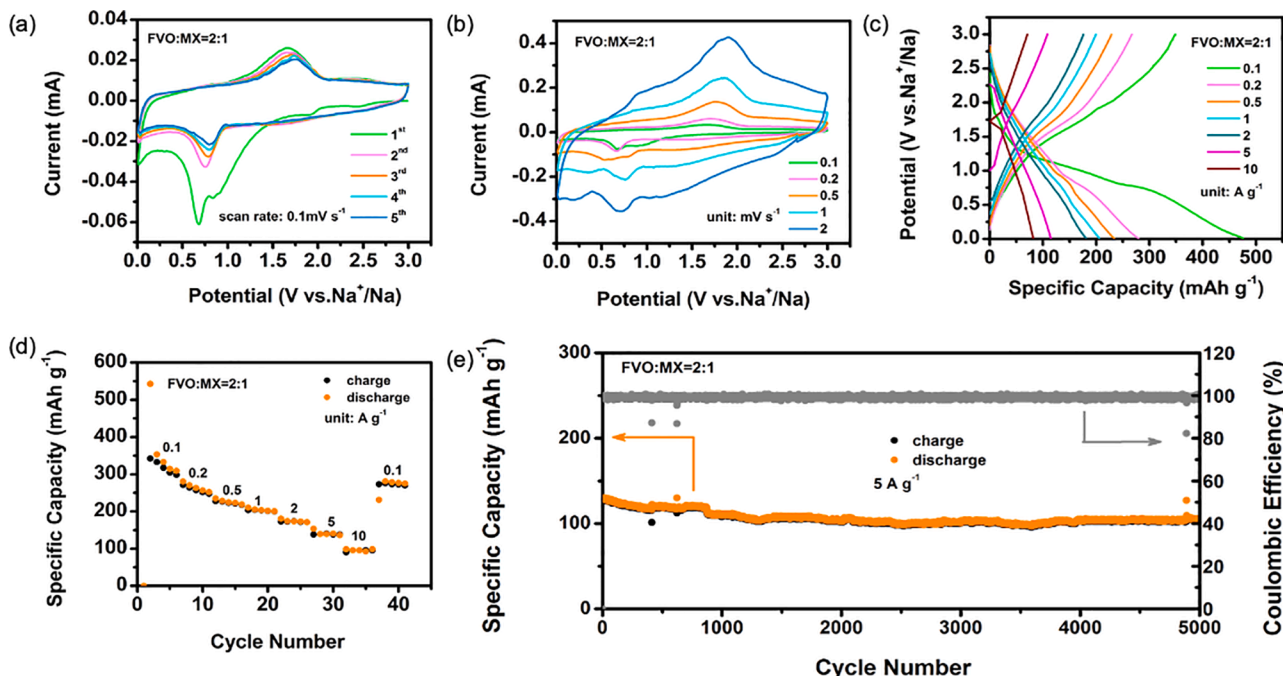


**Fig. 7.** Electrochemical Na-ion storage behavior of FVO/MX = 2:1 electrode. Cyclic voltammograms of a) the initial five cycles at  $0.1 \text{ mV s}^{-1}$  and b) at  $0.1 \text{ mV s}^{-1}$  to  $2 \text{ mV s}^{-1}$ . c) Charge and discharge profiles at different current density from  $0.1 \text{ A g}^{-1}$  to  $10 \text{ A g}^{-1}$ . d) Rate performance and e) Long cycling test for FVO/MX = 2:1 at  $5 \text{ A g}^{-1}$ .

## Declaration of Competing Interest

The authors declare that they have no known competing financial interests or personal relationships that could have appeared to influence the work reported in this paper.

## Acknowledgements

This work was financially supported by National Natural Science of China (No.22179048) and the Science & Technology Department of Jilin Province (No.20210402070GH).

## Appendix A. Supplementary data

Supplementary data to this article can be found online at <https://doi.org/10.1016/j.cej.2022.135012>.

## References

- [1] J. Piatek, S. Afyon, T.M. Budnyak, S. Budnyk, M.H. Sipponen, A. Slabon, Sustainable Li-Ion batteries: chemistry and recycling, *Adv. Energy Mater.* 11 (43) (2021) 2003456, <https://doi.org/10.1002/aenm.202003456>.
- [2] Y. Balali, S. Stegen, Review of energy storage systems for vehicles based on technology, environmental impacts, and costs, *Renew. Sust. Energ. Rev.* 135 (1) (2021), 110185, <https://doi.org/10.1016/j.rser.2020.110185>.
- [3] L.-F. Zhou, D. Yang, T. Du, H. Gong, W.-B. Luo, The current process for the recycling of spent lithium ion batteries, *Front. Chem.* 8 (1) (2020), 578044, <https://doi.org/10.3389/fchem.2020.578044>.
- [4] B. Moradi, G.G. Botte, Recycling of graphite anodes for the next generation of lithium ion batteries, *J. Appl. Electrochem.* 46 (2) (2016) 123–148, <https://doi.org/10.1007/s10800-015-0914-0>.
- [5] H.Y. Wang, T. Ikeda, K. Fukuda, M. Yoshio, Effect of milling on the electrochemical performance of natural graphite as an anode material for lithium-ion battery, *J. Power Sources* 83 (1–2) (1999) 141–147, [https://doi.org/10.1016/s0378-7753\(99\)00288-8](https://doi.org/10.1016/s0378-7753(99)00288-8).
- [6] Y. Yu, L. Gu, C. Zhu, S. Tsukimoto, P.A. van Aken, J. Maier, Reversible storage of lithium in silver-coated three-dimensional macroporous silicon, *Adv. Mater.* 22 (20) (2010) 2247–2250, <https://doi.org/10.1002/adma.200903755>.
- [7] G. Kucinskis, G. Bajars, J. Kleperis, Graphene in lithium ion battery cathode materials: A review, *J. Power Sources* 240 (1) (2013) 66–79, <https://doi.org/10.1016/j.jpowsour.2013.03.160>.
- [8] H. Jia, X. Li, J. Song, X. Zhang, L. Luo, Y. He, B. Li, Y. Cai, S. Hu, X. Xiao, C. Wang, K.M. Rosso, R. Yi, R. Patel, J.-G. Zhang, Hierarchical porous silicon structures with extraordinary mechanical strength as high-performance lithium-ion battery anodes, *Nat. Commun.* 11 (1) (2020) 1474, <https://doi.org/10.1038/s41467-020-15217-9>.
- [9] G. Liang, X. Qin, J. Zou, L. Luo, Y. Wang, M. Wu, H. Zhu, G. Chen, F. Kang, B. Li, Electrosprayed silicon-embedded porous carbon microspheres as lithium-ion battery anodes with exceptional rate capacities, *Carbon* 127 (1) (2017) 424–431, <https://doi.org/10.1016/j.carbon.2017.11.013>.
- [10] C.K. Chan, H. Peng, G. Liu, K. McIlwrath, X.F. Zhang, R.A. Huggins, Y. Cui, High-performance lithium battery anodes using silicon nanowires, *Nat. Nanotechnol.* 3 (1) (2008) 31–35, <https://doi.org/10.1038/nnano.2007.411>.
- [11] I.H. Son, J.H. Park, S. Kwon, S. Park, M.H. Ruemmeli, A. Bachmatiuk, H.J. Song, J. Ku, J.W. Choi, J.-M. Choi, S.-G. Do, H. Chang, Silicon carbide-free graphene growth on silicon for lithium-ion battery with high volumetric energy density, *Nat. Commun.* 6 (1) (2015) 7393, <https://doi.org/10.1038/ncomms8393>.
- [12] S. Dong, Y. Song, Y. Fang, K. Zhu, K. Ye, Y. Gao, J. Yan, G. Wang, D. Cao, Microwave-assisted synthesis of carbon dots modified graphene for full carbon-based potassium ion capacitors, *Carbon* 178 (1) (2021) 1–9, <https://doi.org/10.1016/j.carbon.2021.02.094>.
- [13] R. Hu, Y. Fang, X. Liu, K. Zhu, D. Cao, J. Yi, G. Wang, Synthesis of SnS<sub>2</sub> ultrathin nanosheets as anode materials for potassium ion batteries, *Chem Res Chin Univ* 37 (2) (2021) 311–317, <https://doi.org/10.1007/s40242-021-0017-x>.
- [14] S. Komaba, Sodium-driven rechargeable batteries: an effort towards future energy storage, *Chem. Lett.* 49 (12) (2020) 1507–1516, <https://doi.org/10.1246/cl.200568>.
- [15] A. Eftekhari, Z. Jian, X. Ji, Potassium secondary batteries, *ACS Appl. Mater. Interfaces* 9 (5) (2017) 4404–4419, <https://doi.org/10.1021/acsmami.6b07989>.
- [16] S. Ni, J. Liu, D. Chao, L. Mai, Vanadate-based materials for Li-ion batteries: the search for anodes for practical applications, *Adv. Energy Mater.* 9 (14) (2019) 1803324, <https://doi.org/10.1002/aenm.201803324>.
- [17] Z. Jian, M. Zheng, Y. Liang, X. Zhang, S. Gheytani, Y. Lan, Y. Shi, Y. Yao, Li<sub>3</sub>VO<sub>4</sub> anchored graphene nanosheets for long-life and high-rate lithium-ion batteries, *Chem. Commun.* 51 (1) (2015) 229–231, <https://doi.org/10.1039/c4cc07444k>.
- [18] S. Zhang, R. Hu, Synthesis and electrochemical performance of CuV<sub>2</sub>O<sub>6</sub>/PEDOT: PSS composite nanobelts as anode materials for lithium-ion batteries, *Mater. Lett.* 176 (1) (2016) 131–134, <https://doi.org/10.1016/j.matlet.2016.04.108>.
- [19] H. Liu, D. Tang, Synthesis of ZnV<sub>2</sub>O<sub>6</sub> powder and its cathodic performance for lithium secondary battery, *Mater. Chem. Phys.* 114 (2–3) (2009) 656–659, <https://doi.org/10.1016/j.matchemphys.2008.10.055>.
- [20] J.-S. Park, J.H. Kim, Y.C. Kang, Synthesis of carbonaceous/carbon-free nanofibers consisted of Co<sub>3</sub>V<sub>2</sub>O<sub>8</sub> nanocrystals for lithium-ion battery anode with ultralong cycle life, *Electrochim. Acta* 313 (1) (2019) 48–58, <https://doi.org/10.1016/j.electacta.2019.04.189>.
- [21] X.G. Niu, Y.C. Zhang, L.L. Tan, Z. Yang, J. Yang, T. Liu, L. Zeng, Y.J. Zhu, L. Guo, Amorphous FeVO<sub>4</sub> as a promising anode material for potassium-ion batteries, *Energy Stor. Mater.* 22 (1) (2019) 160–167, <https://doi.org/10.1016/j.ensm.2019.01.011>.
- [22] H. Zhang, K. Ye, K. Zhu, R. Cang, J. Yan, K. Cheng, G. Wang, D. Cao, The FeVO<sub>4</sub>x0.9H<sub>2</sub>O/Graphene composite as anode in aqueous magnesium ion battery, *Electrochim. Acta* 256 (1) (2017) 357–364, <https://doi.org/10.1016/j.electacta.2017.10.038>.
- [23] S. Denis, R. Dedryvere, E. Baudrin, S. Laruelle, M. Touboul, J. Olivier-Fourcade, J. C. Jumas, J.M. Tarascon, Fe-57 Mossbauer study of the electrochemical reaction of lithium with triclinic iron vanadate, *Chem. Mater.* 12 (12) (2000) 3733–3739, <https://doi.org/10.1021/cm001084d>.
- [24] H. Zhang, K. Ye, K. Zhu, R. Cang, J. Yan, K. Cheng, G. Wang, D. Cao, High-energy-density aqueous magnesium-ion battery based on a carbon-coated FeVO<sub>4</sub> Anode and a Mg-OMS-1 Cathode, *Chem-Eur J* 23 (67) (2017) 17118–17126, <https://doi.org/10.1002/chem.201703806>.
- [25] X.-H. Ma, F. Zhang, Y.-Y. Wei, J.-H. Zhou, J. Wang, W. Jia, Z.-F. Zi, J.-M. Dai, Facile synthesis of amorphous FeVO<sub>4</sub> nanoparticles as novel cathode materials for sodium-ion batteries, *J. Alloys Compd.* 768 (1) (2018) 181–189, <https://doi.org/10.1016/j.jallcom.2018.07.249>.
- [26] X. Liu, Y. Cao, H. Zheng, C. Feng, Synthesis and electrochemical performances of FeVO<sub>4</sub>H<sub>2</sub>O and FeVO<sub>4</sub>H<sub>2</sub>O/graphene as novel anode materials, *Mater. Lett.* 187 (1) (2017) 15–19, <https://doi.org/10.1016/j.matlet.2016.10.022>.
- [27] Q. Wei, Q. Li, Y. Jiang, Y. Zhao, S. Tan, J. Dong, L. Mai, D.-L. Peng, High-energy and high-power pseudocapacitor-battery hybrid sodium-ion capacitor with Na<sup>+</sup> Intercalation pseudocapacitance anode, *Nano-Micro Lett* 13 (1) (2021) 55, <https://doi.org/10.1007/s40820-020-00567-2>.
- [28] J. Dong, Y. He, Y. Jiang, S. Tan, Q. Wei, F. Xiong, Z. Chu, Q. An, L. Mai, Intercalation pseudocapacitance of FeVO<sub>4</sub>·nH<sub>2</sub>O nanowires anode for high-energy and high-power sodium-ion capacitor, *Nano Energy* 73 (1) (2020), 104838, <https://doi.org/10.1016/j.nanoen.2020.104838>.
- [29] Q. Wei, R.H. DeBlock, D.M. Butts, C. Choi, B. Dunn, Pseudocapacitive vanadium-based materials toward high-rate sodium-ion storage, *Energy & Environmental Materials* 3 (3) (2020) 221–234, <https://doi.org/10.1002/eem2.12131>.
- [30] A.S. Levitt, M. Alhabeb, C.B. Hatter, A. Sarycheva, G. Dion, Y. Gogotsi, *Electrospun MXene/carbon nanofibers as supercapacitor electrodes*, *J. Mater. Chem. A* 7 (1) (2019) 269–277, <https://doi.org/10.1039/c8ta09810g>.
- [31] B. Anasori, M.R. Lukatskaya, Y. Gogotsi, 2D metal carbides and nitrides (MXenes) for energy storage, *Nat. Rev. Mater.* 2 (2) (2017) 16098, <https://doi.org/10.1038/natrevmats.2016.98>.
- [32] M. Naguib, O. Mashtalar, J. Carle, V. Presser, J. Lu, L. Hultman, Y. Gogotsi, M. W. Barsoum, Two-dimensional transition metal carbides, *ACS Nano* 6 (2) (2012) 1322–1331, <https://doi.org/10.1021/nn204153h>.
- [33] D. Lei, N. Liu, T. Su, L. Wang, J. Su, Z. Zhang, Y. Gao, Research progress of MXenes-based wearable pressure sensors, *Appl. Materials 8* (11) (2020) 110702, <https://doi.org/10.1063/5.0026984>.
- [34] K. Huang, Z. Li, J. Lin, G. Han, P. Huang, Two-dimensional transition metal carbides and nitrides (MXenes) for biomedical applications, *Chem. Soc. Rev.* 47 (14) (2018) 5109–5124, <https://doi.org/10.1039/c7cs00838d>.
- [35] F. Shahzad, M. Alhabeb, C.B. Hatter, B. Anasori, S.M. Hong, C.M. Koo, Y. Gogotsi, Electromagnetic interference shielding with 2D transition metal carbides (MXenes), *Science* 353 (6304) (2016) 1137–1140, <https://doi.org/10.1126/science.aag2421>.
- [36] J. Nan, X. Guo, J. Xiao, X. Li, W. Chen, W. Wu, H. Liu, Y. Wang, M. Wu, G. Wang, Nanoengineering of 2D MXene-based materials for energy storage applications, *Small* 17 (9) (2021) 1902085, <https://doi.org/10.1002/smll.201902085>.
- [37] L. Gao, C. Li, W. Huang, S. Mei, H. Lin, Q. Ou, Y. Zhang, J. Guo, F. Zhang, S. Xu, H. Zhang, MXene/Polymer membranes: synthesis, properties, and emerging applications, *Chem. Mater.* 32 (5) (2020) 1703–1747, <https://doi.org/10.1021/acs.chemmater.9b04408>.
- [38] B. Cao, H. Liu, P. Zhang, N. Sun, B. Zheng, Y. Li, H. Du, B. Xu, Flexible MXene framework as a fast electron/potassium-ion dual-function conductor boosting stable potassium storage in graphite electrodes, *Adv. Funct. Mater.* 31 (32) (2021) 2102126, <https://doi.org/10.1002/adfm.202102126>.
- [39] P. Zhang, Q. Zhu, Z. Guan, Q. Zhao, N. Sun, B. Xu, A flexible Si@C electrode with excellent stability employing an MXene as a multifunctional binder for lithium-ion batteries, *ChemSusChem* 13 (6) (2020) 1621–1628, <https://doi.org/10.1002/adfm.202102126>.
- [40] Q. Zhao, Q. Zhu, J. Miao, P. Zhang, B. Xu, 2D MXene nanosheets enable small-sulfur electrodes to be flexible for lithium-sulfur batteries, *Nanoscale* 11 (17) (2019) 8442–8448, <https://doi.org/10.1039/C8NR09653H>.
- [41] C. Zhang, S.-N. Park, A. Seral-Ascaso, S. Barwich, N. McEoy, C.S. Boland, J. N. Coleman, Y. Gogotsi, V. Nicolosi, High capacity silicon anodes enabled by MXene viscous aqueous ink, *Nat. Commun.* 10 (1) (2019) 849, <https://doi.org/10.1038/s41467-019-08383-y>.
- [42] H. Zhang, Z.H. Fu, D. Legut, T.C. Germann, R.F. Zhang, Stacking stability and sliding mechanism in weakly bonded 2D transition metal carbides by van der Waals force, *RSC Adv.* 7 (88) (2017) 55912–55919, <https://doi.org/10.1039/c7ra11139h>.

- [43] K. Li, M. Liang, H. Wang, X. Wang, Y. Huang, J. Coelho, S. Pinilla, Y. Zhang, F. Qi, V. Nicolosi, Y. Xu, 3D MXene architectures for efficient energy storage and conversion, *Adv. Funct. Mater.* 30 (47) (2020) 2000842, <https://doi.org/10.1002/adfm.202000842>.
- [44] Y. Tian, Y. An, J. Feng, Flexible and freestanding silicon/mxene composite papers for high-performance lithium-ion batteries, *ACS Appl. Mater. Interfaces* 11 (10) (2019) 10004–10011, <https://doi.org/10.1021/acsami.8b2189310.1021/acsami.8b21893.s001>.
- [45] N. Sun, Q. Zhu, B. Anasori, P. Zhang, H. Liu, Y. Gogotsi, B. Xu, MXene-Bonded flexible hard carbon film as anode for stable Na/K-ion storage, *Adv. Funct. Mater.* 29 (51) (2019) 1906282, <https://doi.org/10.1002/adfm.201906282>.
- [46] X. Liu, Y. Cao, H. Zheng, X. Chen, C. Feng, Synthesis and modification of FeVO<sub>4</sub> as novel anode for lithium-ion batteries, *Appl. Surf. Sci.* 394 (1) (2017) 183–189, <https://doi.org/10.1016/j.apsusc.2016.09.133>.
- [47] A. Sarycheva, Y. Gogotsi, Raman spectroscopy analysis of the structure and surface chemistry of Ti<sub>3</sub>C<sub>2</sub>T<sub>x</sub> MXene, *Chem. Mater.* 32 (8) (2020) 3480–3488, <https://doi.org/10.1021/acs.chemmater.0c0035910.1021/acs.chemmater.0c00359.s001>.
- [48] K. Wang, X. Zhu, C. Wang, Y. Hu, L. Gu, S. Qiu, X. Gao, Y. Mao, Self-standing hybrid film of SnO<sub>2</sub> nanotubes and mxene as a high-performance anode material for thin film lithium-ion batteries, *ChemistrySelect* 4 (41) (2019) 12099–12103, <https://doi.org/10.1002/slct.201903537>.
- [49] F. Cheng, J. Chen, Transition metal vanadium oxides and vanadate materials for lithium batteries, *J. Mater. Chem.* 21 (27) (2011) 9841–9848, <https://doi.org/10.1039/c0jm04239k>.
- [50] N. Meddings, M. Heinrich, F. Overney, J.-S. Lee, V. Ruiz, E. Napolitano, S. Seitz, G. Hinds, R. Raccichini, M. Gabers, J. Park, Application of electrochemical impedance spectroscopy to commercial Li-ion cells: A review, *J. Power Sources* 480 (1) (2020), 228742, <https://doi.org/10.1016/j.jpowsour.2020.228742>.
- [51] V.D. Nithya, R.K. Selvan, Synthesis, electrical and dielectric properties of FeVO<sub>4</sub> nanoparticles, *Physica B* 406 (1) (2011) 24–29, <https://doi.org/10.1016/j.physb.2010.10.004>.
- [52] K.Z. Cao, L.F. Jiao, H.Q. Liu, Y.C. Liu, Y.J. Wang, Z.P. Guo, H.T. Yuan, 3D hierarchical porous alpha-Fe<sub>2</sub>O<sub>3</sub> Nanosheets for high-performance lithium-ion batteries, *Adv. Energy Mater.* 5 (4) (2015) 1401421, <https://doi.org/10.1002/aenm.201401421>.
- [53] Y. Sun, X. Hu, W. Luo, F. Xia, Y. Huang, Reconstruction of conformal nanoscale mno on graphene as a high-capacity and long-life anode material for lithium ion batteries, *Adv. Funct. Mater.* 23 (19) (2013) 2436–2444, <https://doi.org/10.1002/adfm.201202623>.
- [54] S.H. Lee, S.H. Yu, J.E. Lee, A.H. Jin, D.J. Lee, N. Lee, H. Jo, K. Shin, T.Y. Ahn, Y. W. Kim, H. Choe, Y.E. Sung, T. Hyeon, Self-assembled Fe<sub>3</sub>O<sub>4</sub> nanoparticle clusters as high-performance anodes for lithium ion batteries via geometric confinement, *Nano Lett.* 13 (9) (2013) 4249–4256, <https://doi.org/10.1021/nl401952h>.
- [55] N. Yan, Y. Xu, H. Li, W. Chen, The preparation of FeVO<sub>4</sub> as a new sort of anode material for lithium ion batteries, *Mater. Lett.* 165 (1) (2016) 223–226, <https://doi.org/10.1016/j.matlet.2015.11.061>.
- [56] J. Luo, J. Zheng, J. Nai, C. Jin, H. Yuan, O. Sheng, Y. Liu, R. Fang, W. Zhang, H. Huang, Y. Gan, Y. Xia, C. Liang, J. Zhang, W. Li, X. Tao, Atomic sulfur covalently engineered interlayers of Ti<sub>3</sub>C<sub>2</sub> mxene for ultra-fast sodium-ion storage by enhanced pseudocapacitance, *Adv. Funct. Mater.* 29 (10) (2019) 1808107, <https://doi.org/10.1002/adfm.201808107>.
- [57] P. Simon, Y. Gogotsi, B. Dunn, Where do batteries end and supercapacitors begin? *Science* 343 (6176) (2014) 1210–1211, <https://doi.org/10.1126/science.1246464>.
- [58] J. Wang, J. Polleux, J. Lim, B. Dunn, Pseudocapacitive contributions to electrochemical energy storage in TiO<sub>2</sub> (anatase) nanoparticles, *J. Phys. Chem. C* 111 (40) (2007) 14925–14931, <https://doi.org/10.1021/jp074464w>.
- [59] T. Brezesinski, J. Wang, S.H. Tolbert, B. Dunn, Ordered mesoporous  $\alpha$ -MoO<sub>3</sub> with iso-oriented nanocrystalline walls for thin-film pseudocapacitors, *Nat. Mater.* 9 (2) (2010) 146–151, <https://doi.org/10.1038/nmat2612>.